

Characteristics of $\text{SrCo}_{1-x}\text{Fe}_x\text{O}_{3-\delta}$ Perovskite Powders with Improved O_2/CO_2 Production Performance for Oxyfuel Combustion

Qiuwan Shen, Ying Zheng,* Cong Luo, and Chuguang Zheng

State Key Laboratory of Coal Combustion, School of Energy and Power Engineering, Huazhong University of Science and Technology, 1037 Luoyu Road, Wuhan 430074, China. *E-mail: zhengying@hust.edu.cn

Received October 6, 2013, Accepted February 5, 2014

Perovskite-type oxides are promising oxygen carriers in producing oxygen-enriched CO_2 gas stream for oxyfuel combustion. In this study, a new series of $\text{SrCo}_{1-x}\text{Fe}_x\text{O}_{3-\delta}$ ($x = 0.2, 0.4, 0.6, 0.8$) was prepared and used to produce O_2/CO_2 mixture gas. The phase, crystal structure, and morphological properties of $\text{SrCo}_{1-x}\text{Fe}_x\text{O}_{3-\delta}$ were investigated through X-ray diffraction, specific surface area measurements, and environmental scanning electron microscopy. The oxygen desorption performance of $\text{SrCo}_{1-x}\text{Fe}_x\text{O}_{3-\delta}$ was studied in a fixed-bed reactor system. Results showed that the different x values of $\text{SrCo}_{1-x}\text{Fe}_x\text{O}_{3-\delta}$ have no obvious effects on crystalline structure. However, the oxygen desorption performance of $\text{SrCo}_{1-x}\text{Fe}_x\text{O}_{3-\delta}$ is improved by Co doping. Moreover, $\text{SrCo}_{0.8}\text{Fe}_{0.2}\text{O}_{3-\delta}$ synthesized *via* a new EDTA method has a larger BET surface area ($40.396 \text{ m}^2/\text{g}$), smaller particle size (48.3 nm), and better oxygen production performance compared with that synthesized through a liquid citrate method.

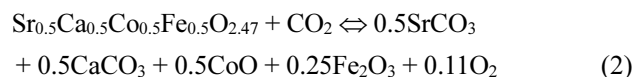
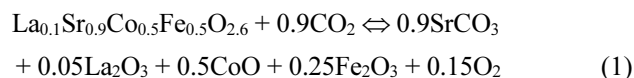
Key Words : Perovskite-type, Crystalline structure, Oxygen desorption, EDTA-citrate

Introduction

Combustion of fossil fuels contributes to the emission of CO_2 into the atmosphere, which consequently causes global warming.¹⁻³ Oxyfuel combustion is one way to achieve zero CO_2 emission. Oxyfuel combustion or O_2/CO_2 recycle combustion is the process in which oxygen is fed to the chamber for combustion and most CO_2 -rich exhaust gas is recycled to maintain the combustion temperature. Oxy-fuel combustion has the following advantages: (1) up to 95% CO_2 concentration in the dry flue gas; (2) improved boiler efficiency; (3) reduced power consumption in flue gas treatment because of the small amount of flue gas involved; and (4) saved denitrogenation equipment and process.^{4,5} However, the high cost of oxygen production limits the implementation of oxy-combustion. Therefore, significant reduction in the cost of oxygen production is important for the viability of oxy-fuel combustion power plants in the future when CO_2 capture becomes a necessity.⁶

Perovskite-type metal oxides have received considerable attention due to their potential applications in photocatalysis, oxygen-permeable membranes, energy storage, gas sensors, superconductivity, and magnetoresistance materials.⁷⁻¹¹ Perovskite-type oxides are capable of acting as oxygen carriers providing pure O_2 or O_2/CO_2 gas streams for oxyfuel combustion.¹²⁻¹⁴ Such oxygen production consists of the two main steps shown in Figure 1: oxygen adsorption and oxygen desorption. In the first step, air is used as feed gas to saturate the perovskite oxygen carrier with O_2 ; in the second step, CO_2 is used as sweep gas to desorb O_2 from the perovskite to produce an O_2 -enriched CO_2 flue gas stream. The reversible adsorption/desorption processes based on the perovskite-type oxygen carriers $\text{La}_{0.1}\text{Sr}_{0.9}\text{Co}_{0.5}\text{Fe}_{0.5}\text{O}_{3-\delta}$ and

$\text{Sr}_{0.5}\text{Ca}_{0.5}\text{Co}_{0.5}\text{Fe}_{0.5}\text{O}_{3-\delta}$ are described as follows:



Fundamental studies on perovskite-type oxides have focused on selection and syntheses of materials and their structural identity and stability, thermal properties, and O_2 adsorption/desorption performance.¹²⁻¹⁴ However, the relatively slow oxygen desorption rate and poor regeneration capacity in this process may be the major drawbacks for this type of materials. This issue hinders the prediction of high O_2 amount in industrial air separation and the sufficient regeneration of sorbent. Therefore, the development of perovskite-type oxygen carrier materials with excellent oxygen desorption performance and cyclic performance is necessary.

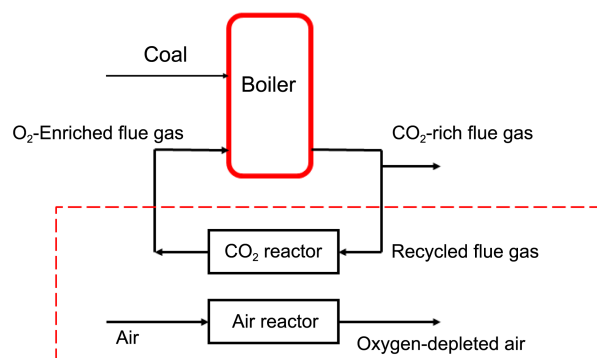


Figure 1. Simplified schematic of O_2/CO_2 production for oxyfuel combustion.

$\text{SrCo}_{1-x}\text{Fe}_x\text{O}_{3-\delta}$ is a promising perovskite that has drawn considerable attention because of its high oxygen permeation flux as dense perovskite ceramic membrane.^{15,16} However, only a few reports have evaluated the use of perovskite as oxygen carrier for oxygen production.¹⁷ To the best of our knowledge, the effects of micro-structure and Co doping of $\text{SrCo}_{1-x}\text{Fe}_x\text{O}_{3-\delta}$ on oxygen production performance remain unknown. Moreover, the development of $\text{SrCo}_{1-x}\text{Fe}_x\text{O}_{3-\delta}$ powders needs further research. This study aims to develop $\text{SrCo}_{1-x}\text{Fe}_x\text{O}_{3-\delta}$ powders with improved O_2/CO_2 production performance for oxyfuel combustion system and to investigate the improvement of oxygen desorption performance for $\text{SrCo}_{1-x}\text{Fe}_x\text{O}_{3-\delta}$ through micro-characteristic and fixed-bed experiments measurements. The effects of Co doping and different synthesis methods are also investigated and reported.

Experimental

The $\text{SrCo}_{1-x}\text{Fe}_x\text{O}_{3-\delta}$ powders used in this study were synthesized *via* a liquid citrate method.¹²⁻¹⁴ The starting materials were $\text{Sr}(\text{NO}_3)_2 \cdot 4\text{H}_2\text{O}$, $\text{Co}(\text{NO}_3)_2 \cdot 6\text{H}_2\text{O}$, $\text{Fe}(\text{NO}_3)_3 \cdot 9\text{H}_2\text{O}$, and citric acid, all of which were of analytical purity. $\text{SrCo}_{1-x}\text{Fe}_x\text{O}_{3-\delta}$ powders were prepared through the following process. Stoichiometric metal nitrate was dissolved in diluted nitric acid aqueous solutions. The molar ratio between the total amount of metal ions and the amount of citric acid was 1:1.5. The precursor solution was heated and stirred at 70 °C until it gelled. The resulting viscous gel was dried at 105 °C for 24 h. Self-ignition was performed at 400 °C to burn out the organic compounds. Finally, the black ash was sintered at 850 °C for 20 h and ground into fine powders for characterization.

Some $\text{SrCo}_{0.8}\text{Fe}_{0.2}\text{O}_{3-\delta}$ samples were also prepared using an ethylenediamine-tetraacetic acid (EDTA)–citrate complex gel method for comparison to understand the effect of synthesis method on the oxygen production properties of $\text{SrCo}_{0.8}\text{Fe}_{0.2}\text{O}_{3-\delta}$.^{15,16,18,19} The detailed procedures to synthesize 0.1 mol of $\text{SrCo}_{0.8}\text{Fe}_{0.2}\text{O}_{3-\delta}$ powders were as follows. First, 0.1 mol of EDTA was mixed with 125 mL of 13 N NH_4OH solution to produce NH_3 –EDTA solution. Then, 0.05 mol of $\text{Sr}(\text{NO}_3)_2 \cdot 4\text{H}_2\text{O}$, 0.04 mol of $\text{Co}(\text{NO}_3)_2 \cdot 6\text{H}_2\text{O}$, and 0.01 mol of $\text{Fe}(\text{NO}_3)_3 \cdot 9\text{H}_2\text{O}$ were dissolved in the NH_3 –EDTA solution. The solution was mixed and prepared, and then 0.15 mol of citric acid was added to the mixed solution. The mole ratio of EDTA: citric acid: total metal ions was 1:1.5:1. Then, the precursor solution was heated and stirred at 70 °C until it gelled. The resulting viscous gel was dried at 105 °C for 24 h and self-ignited at 400 °C for 4 h to burn out the organic compounds. Finally, the black ash was sintered at 850 °C for 20 h and ground into fine powders for characterization. Except for some special notifications, all results were based on the samples synthesized through liquid citrate method in this study.

The phase composition of the samples was determined by X-ray diffraction (XRD, PANalytical B.V.) with $\text{Cu K}\alpha$ radiation ($\lambda = 0.1542$ nm) and a 2θ range of 20–80° with a scanning step of 0.02°. The Rietveld refinements²⁰ were

carried out with GSAS software, which is specially designed to simultaneously refine both structural and micro structural parameters using the least-square method. The peak profile function was modeled using the convolution of the Thompson-Cox-Hastings pseudo-Voigt with the asymmetry function described by Finger *et al.*^{20,21} The particle sizes and lattice distortion of some samples were investigated based on Fourier analysis of their XRD peaks using Eqs. (3) and Eqs. (4), respectively.

$$D = \frac{k \times \lambda}{\beta \times \cos \theta} \quad (3)$$

$$\varepsilon = \frac{\beta}{4 \tan \theta} \quad (4)$$

where D is the average particle size in nm, λ is the $\text{CuK}\alpha$ radiation wavelength ($\lambda = 1.542$ Å), β is the half-width of the peak in radians and θ is the corresponding diffraction angle. k is taken as 0.89 for half maximum line breadth and if the integral line breadth is used, k increases to 0.94.

The morphologies of the synthesized powders were investigated by environmental scanning electron microscopy (ESEM, QUANTA 200, FEI Inc.) A Gemini Micromeritics analyzer (Micromeritics ASAP 2020 instrument, Micromeritics Instrument Corporation, Norcross, USA) was used for Brunauer-Emmett-Teller (BET) surface area measurements.

Oxygen adsorption/desorption experiments were performed in a fixed-bed reactor system, as shown in Figure 2. This system consisted of a gas feeding system, a tube furnace with a quartz reactor, a gas analyzer (Gasboard 3100), and a computerized data acquisition system. The oxygen concentration during desorption was recorded to investigate the oxygen adsorption/desorption performance of the perovskite powders. Approximately 0.5 g of powders was packed in the middle of the quartz reactor. Air and CO_2 were respectively used as feed gas for adsorption and sweep gas for desorption.

In adsorption, the powders were heated to a desired adsorption temperature in a flow of air in 1 atm at a flow rate of 100 mL/min for 20 min. Adsorption was followed by desorption with a switch of the sweep gas from air to CO_2 stream at a flow rate of 50 mL/min. Then, the temperature was set to

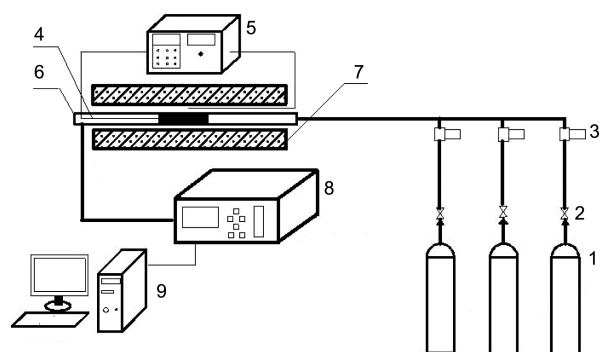


Figure 2. Schematic of fixed-bed reaction system. (1) Gas cylinder; (2) valve; (3) flow controller; (4) thermocouple; (5) temperature controller; (6) quartz reactor; (7) horizontal tube furnace; (8) gas analyzer; and (9) data acquisition system.

the predetermined desorption temperature. The desorption step was stopped when the O_2 concentration nearly dropped to zero. Then, the CO_2 stream was switched to air to start the next cycle of oxygen adsorption and desorption.

Results and Discussion

Sample Characteristics and Effects of Co Doping for $\text{SrCo}_{1-x}\text{Fe}_x\text{O}_{3-\delta}$. X-ray diffraction (XRD) patterns of the synthesized perovskite samples are shown in Figure 3. XRD studies show that all samples are single phase and have cubic perovskite-type structure with Pm3m space group. The results of Rietveld refinement and lattice parameters are given in Table 1. The different concentrations of Fe ions in the B-site do not cause obvious changes in crystalline structure. However, slight changes are observed in the unit cell parameters of $\text{SrCo}_{0.8}\text{Fe}_{0.2}\text{O}_{3-\delta}$, $\text{SrCo}_{0.6}\text{Fe}_{0.4}\text{O}_{3-\delta}$, $\text{SrCo}_{0.4}\text{Fe}_{0.6}\text{O}_{3-\delta}$, and $\text{SrCo}_{0.2}\text{Fe}_{0.8}\text{O}_{3-\delta}$. This result can be attributed to the different sizes between Fe ion radius (0.55 Å) and Co ion radius (0.545 Å). Figures 4(a) and 4(b) compare the fresh $\text{SrCo}_{0.8}\text{Fe}_{0.2}\text{O}_{3-\delta}$ and the products of the sample that undergoes desorption with CO_2 as desorption gas at 850 °C. The XRD pattern of the fresh $\text{SrCo}_{0.8}\text{Fe}_{0.2}\text{O}_{3-\delta}$ shows all the main characteristic peaks of a perovskite phase. Meanwhile, the XRD pattern of the solid products of the carbonation reaction of $\text{SrCo}_{0.8}\text{Fe}_{0.2}\text{O}_{3-\delta}$ shows the main characteristic peaks of SrCO_3 , along with the rest of CoO , Fe_2O_3 , and basically no perovskite phase. This result indicates that the conversion of carbonation reaction for $\text{SrCo}_{0.8}\text{Fe}_{0.2}\text{O}_{3-\delta}$ is relatively very high. Figure 4(c) shows the XRD pattern of a reverted product after 20 cycles of adsorption and desorption. The XRD pattern of the reverted product shows all the main characteristic peaks of a perovskite structure. This result indicates that the solid product after desorption can revert into a perovskite structure through adsorption.

Figure 5 shows oxygen desorption (adsorption and desorption temperatures were both 750 °C) curves of $\text{SrCo}_{1-x}\text{Fe}_x\text{O}_{3-\delta}$ ($x = 0.2, 0.4, 0.6, 0.8$) with different x values. As shown in Figure 5, the Fe ion concentration in the B-site has a

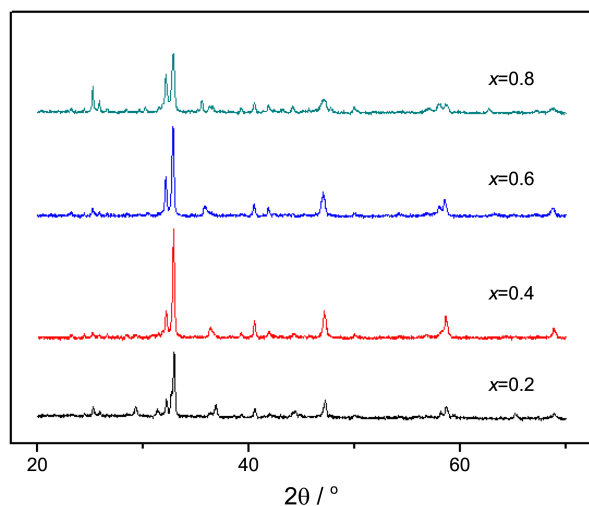


Figure 3. XRD patterns of $\text{SrCo}_{1-x}\text{Fe}_x\text{O}_{3-\delta}$ ($x = 0.2, 0.4, 0.6, 0.8$).

Table 1. Results of Rietveld refinement and lattice parameters

Sample	Structure	a (Å)	Volume (Å ³)	Rp	Rwp
$\text{SrCo}_{0.8}\text{Fe}_{0.2}\text{O}_{3-\delta}$	Cubic Pm3m	3.856593	57.360	0.0423	0.0625
$\text{SrCo}_{0.6}\text{Fe}_{0.4}\text{O}_{3-\delta}$	Cubic Pm3m	3.858037	57.425	0.0408	0.0621
$\text{SrCo}_{0.4}\text{Fe}_{0.6}\text{O}_{3-\delta}$	Cubic Pm3m	3.866531	57.805	0.0487	0.0790
$\text{SrCo}_{0.2}\text{Fe}_{0.8}\text{O}_{3-\delta}$	Cubic Pm3m	3.876721	58.263	0.0497	0.0545

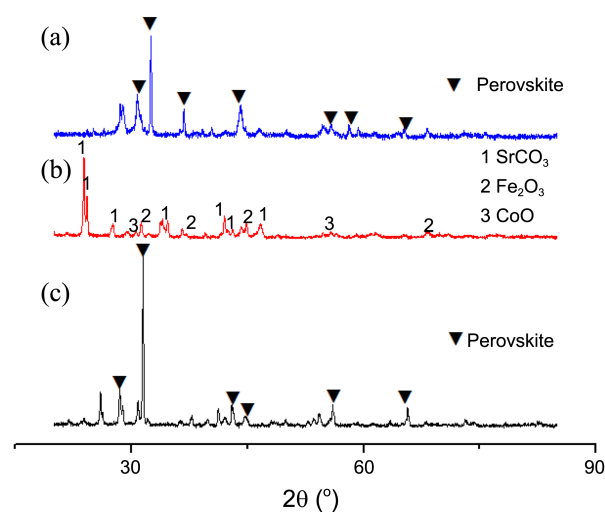


Figure 4. XRD patterns of (a) fresh $\text{SrCo}_{0.8}\text{Fe}_{0.2}\text{O}_{3-\delta}$ calcined at 850 °C; (b) reaction products with CO_2 as desorption gas at 850 °C; (c) reverted products of $\text{SrCo}_{0.8}\text{Fe}_{0.2}\text{O}_{3-\delta}$ after carbonation at 850 °C.

significant effect on the oxygen desorption performance of $\text{SrCo}_{1-x}\text{Fe}_x\text{O}_{3-\delta}$. The slope of the oxygen desorption curve decreases as Fe concentration increases and as x increases from 0.2 to 0.8. The slope of the curve demonstrates the carbonation reaction rate between $\text{SrCo}_{1-x}\text{Fe}_x\text{O}_{3-\delta}$ and CO_2 ,

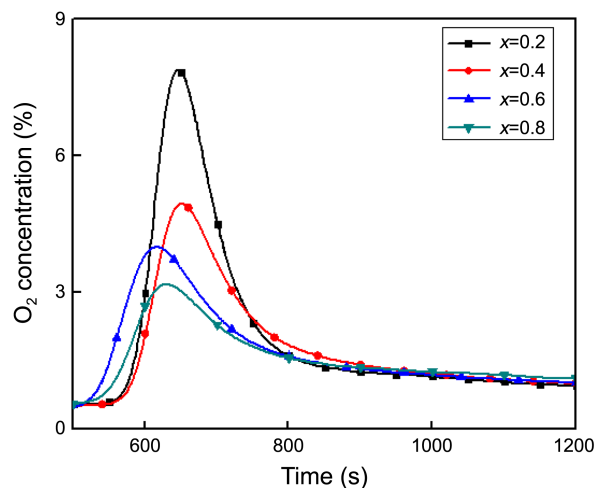


Figure 5. Oxygen desorption curves for $\text{SrCo}_{1-x}\text{Fe}_x\text{O}_{3-\delta}$ ($x = 0.2, 0.4, 0.6, 0.8$).

Table 2. Oxygen desorption amount of a unit mass of SrCo_{1-x}Fe_xO_{3-δ} (x = 0.2, 0.4, 0.6, 0.8)

SrCo _{1-x} Fe _x O _{3-δ}	x = 0.2	x = 0.4	x = 0.6	x = 0.8
Oxygen desorption amount (mg O ₂ /g-sample)	25.27	21.93	21.04	19.25

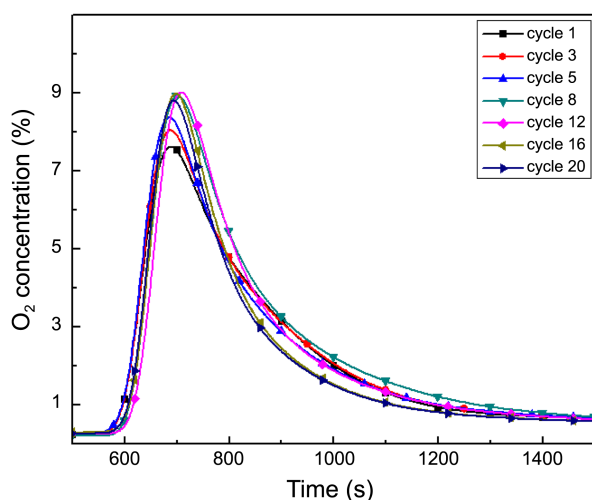
i.e., the oxygen desorption rate of SrCo_{1-x}Fe_xO_{3-δ} during the desorption process. The oxygen desorption amount was calculated by the integral scheme based on the obtained oxygen concentration distribution. The following equation can be used:

$$m_{O_2} = \frac{\Sigma C_{O_2} \times F_{out} \times M_{O_2}}{V_m \times m} \quad (5)$$

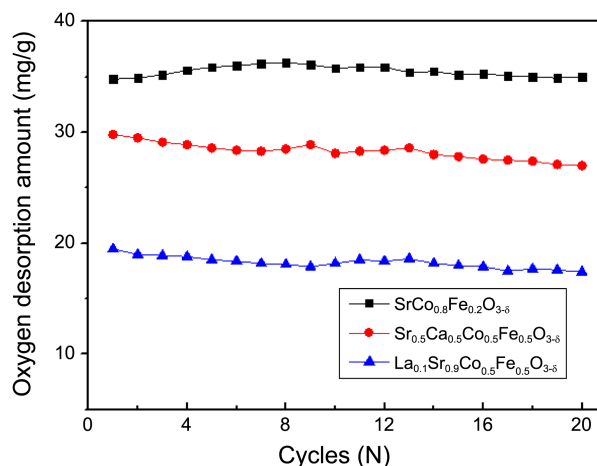
where ΣC_{O_2} is the integration of the entire oxygen concentration during desorption and F_{out} (mL/s) is the flow rate of desorption effluent. We suppose that $F_{out} \approx F_{CO_2}$, M_{O_2} (g/mol) is the molecular weight of O₂, m (g) is the mass of perovskite sample, and m_{O_2} (g/g-sample) is the oxygen desorption amount for 1 g of perovskite sample.

The oxygen desorption amounts for SrCo_{1-x}Fe_xO_{3-δ} (x = 0.2, 0.4, 0.6, 0.8) are shown in Table 2. The values of oxygen desorption amount increase from 19.25 mg/g to 25.27 mg/g with increasing Co doping. Compared with the others, SrCo_{0.8}Fe_{0.2}O_{3-δ} exhibits the highest oxygen desorption amount of 25.27 mg/g. Clearly, the optimum composition for SrCo_{1-x}Fe_xO_{3-δ} with the best oxygen desorption performance is SrCo_{0.8}Fe_{0.2}O_{3-δ}. Therefore, SrCo_{0.8}Fe_{0.2}O_{3-δ} was used for further research.

Cyclic Behavior of the Oxygen Carrier. As promising oxygen carriers that provide stable O₂/CO₂ cycle gas for oxyfuel combustion, perovskite-type oxygen carriers require not only high oxygen desorption amount but also long life and high durability. Figure 9 compares the oxygen desorption curves of 20 continuous cycles of SrCo_{0.8}Fe_{0.2}O_{3-δ}. For each cycle, the adsorption and desorption temperatures were both 850 °C, and the adsorption time was 15 min. As shown

**Figure 6.** Comparison of 20 cycles of oxygen desorption curves (adsorption at 850 °C, desorption at 850 °C).**Table 3.** Twenty cycles of oxygen desorption amount of SCF

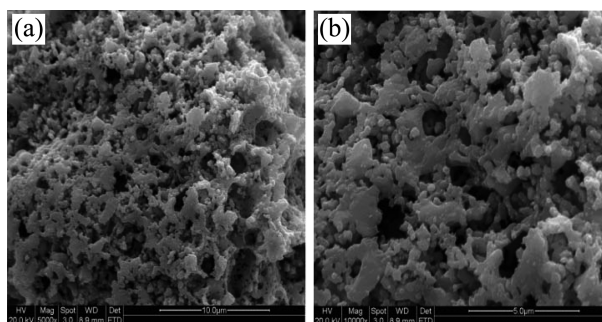
Cycle (N)	1	3	5	8	12	16	20
Oxygen desorption amount (mg O ₂ /g-sample)	34.8	35.2	35.9	36.3	35.9	35.3	35.0

**Figure 7.** Oxygen desorption amount of a unit mass of SrCo_{0.8}Fe_{0.2}O_{3-δ}, Sr_{0.5}Ca_{0.5}Co_{0.5}Fe_{0.5}O_{3-δ} and La_{0.1}Sr_{0.9}Co_{0.5}Fe_{0.5}O_{3-δ} with the number of cycles.

in Figure 6, the cyclic reaction ability of the SrCo_{0.8}Fe_{0.2}O_{3-δ} oxygen carrier does not decline sharply with the number of cycles. As shown in Table 3, the oxygen desorption amount increases to 36.3 mg/g during the first eight cycles and then essentially maintains a constant value during cycles 12 to 20 with some random increase or decrease within the range of experimental error. The oxygen desorption capacity does not obviously decrease with the number of cycles. Therefore, the perovskite-type oxygen carrier SrCo_{0.8}Fe_{0.2}O_{3-δ} has excellent regeneration capacity in cyclic use, which is important for practical applications.

The comparison of cyclic performance between SCF182 and the reference oxygen carriers La_{0.1}Sr_{0.9}Co_{0.5}Fe_{0.5}O_{3-δ} and Sr_{0.5}Ca_{0.5}Co_{0.5}Fe_{0.5}O_{3-δ} is shown in Figure 7. SrCo_{0.8}Fe_{0.2}O_{3-δ} has significantly higher performance than La_{0.1}Sr_{0.9}Co_{0.5}Fe_{0.5}O_{3-δ} and Sr_{0.5}Ca_{0.5}Co_{0.5}Fe_{0.5}O_{3-δ} on cyclic oxygen desorption.

Figures 8 and 9 compare the morphologies of the powder

**Figure 8.** ESEM images of various magnifications for fresh SCF182 calcined at 850 °C: (a) 5000×; (b) 10000×.

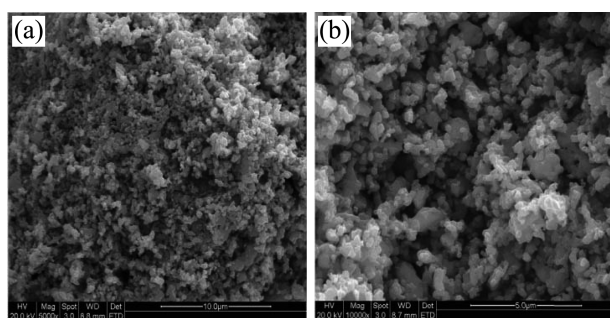


Figure 9. ESEM images of various magnifications for SCF182 after 20 cycles of adsorption/desorption: (a) 5000 \times ; (b) 10000 \times .

particles of the fresh $\text{SrCo}_{0.8}\text{Fe}_{0.2}\text{O}_{3-\delta}$ samples and the samples after 20 cycles of oxygen adsorption and desorption. As shown in Figure 14, the fresh grains are not uniform in shape and the nano-sized crystallites merge to form a porous structure. The porous surface of this structure contributes to the rapid chemical reaction rate during carbonation. As shown in Figure 9, after 20 cycles of adsorption/desorption, the particles exhibit a dense microstructure with small and uniform pores. These particles are more spherical in shape compared with the fresh $\text{SrCo}_{0.8}\text{Fe}_{0.2}\text{O}_{3-\delta}$ particles and demonstrate a hard agglomerate-free nature. The slight decrease in oxygen desorption amount for $\text{SrCo}_{0.8}\text{Fe}_{0.2}\text{O}_{3-\delta}$ after eight cycles could be caused by the pore and surface structure changes in the sample.

Effects of Synthesis Method. Therefore, $\text{SrCo}_{0.8}\text{Fe}_{0.2}\text{O}_{3-\delta}$ was selected as candidate for further research. Different synthesis methods were investigated to improve the oxygen desorption performance of $\text{SrCo}_{0.8}\text{Fe}_{0.2}\text{O}_{3-\delta}$.

The performance of perovskite-type oxygen carriers is closely associated with the related preparation methods. Several methods were used to synthesize perovskite-type powders. These methods include liquid citrate method, EDTA–citrate complex gel method,^{22,23} solid-state reaction method,^{24,25} wet chemical synthesis,²⁶ and sol–gel method.^{27,28}

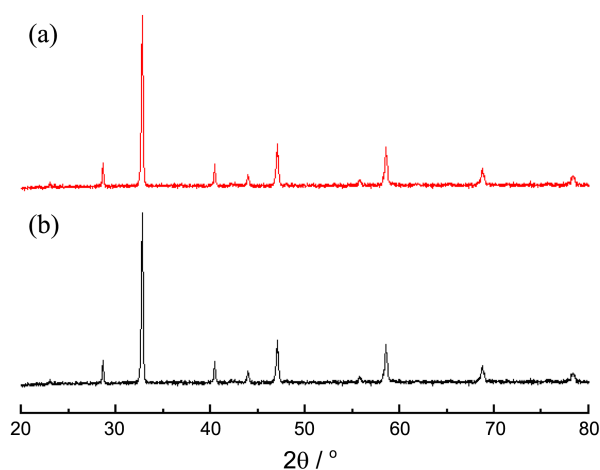


Figure 10. XRD patterns for the powders synthesized through different methods: (a) liquid citrate; (b) EDTA–citrate complex gel method.

Table 4. Particle size, lattice distortion, and BET surface area of $\text{SrCo}_{0.8}\text{Fe}_{0.2}\text{O}_{3-\delta}$ powders synthesized through different methods

$\text{SrCo}_{0.8}\text{Fe}_{0.2}\text{O}_{3-\delta}$	Particle size (nm)	Lattice distortion (%)	BET (m^2/g)
Liquid citrate method	52.4	0.245	34.229
EDTA method	48.3	0.258	40.396

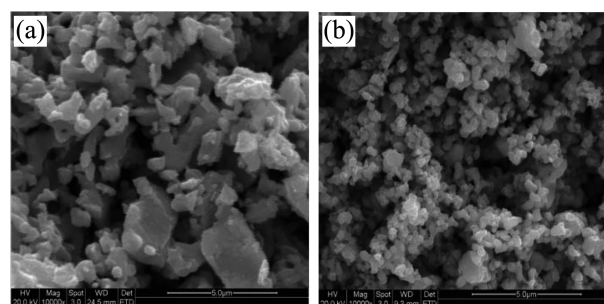


Figure 11. ESEM images of $\text{SrCo}_{0.8}\text{Fe}_{0.2}\text{O}_{3-\delta}$ powders synthesized by (a) the liquid citrate method; (b) the EDTA–citrate complex gel method.

Among these methods, the EDTA–citrate complex gel method is expected to produce a more uniform mixing of the metal elements at the molecular level, thus yielding a more uniform microstructure of the final particles. This method could be used to synthesize homogeneous, high-purity, and crystalline oxide powders.

Figure 10 shows the XRD patterns of $\text{SrCo}_{0.8}\text{Fe}_{0.2}\text{O}_{3-\delta}$ synthesized *via* the liquid citrate method in the reference¹⁷ and the EDTA–citrate complex gel (EDTA) method. XRD characterizations show that pure perovskite structures are formed for powders synthesized *via* both methods. The major diffraction peaks of the as-synthesized powders were matched with the theoretical ones.

The particle size and lattice distortion for the synthesized samples were calculated from the XRD data, as shown in Table 4. As shown in Table 4, the synthesis method affects the particle size. The EDTA method produces smaller particle size and larger lattice distortion over the liquid citrate method. The higher value of the lattice distortion parameter may be associated to the smaller size and relatively free energy of the particles.¹⁷

The morphologies of the synthesized perovskite powders were studied by ESEM. Figure 11 shows a comparison between the ESEM images of $\text{SrCo}_{0.8}\text{Fe}_{0.2}\text{O}_{3-\delta}$ samples prepared through different methods. The ESEM images show that the synthesis method significantly affects the morphologies of the resulting perovskite powders. $\text{SrCo}_{0.8}\text{Fe}_{0.2}\text{O}_{3-\delta}$ prepared through the traditional liquid citrate method is composed of agglomerations of larger particles of irregular shape and smooth surface. $\text{SrCo}_{0.8}\text{Fe}_{0.2}\text{O}_{3-\delta}$ synthesized *via* the EDTA method is composed of particles that are relatively ordered and groups of numerous spherical crystallites, leading to the formation of a relatively condensed and compact surface. Meanwhile, the morphology, microstructure, and pore distri-

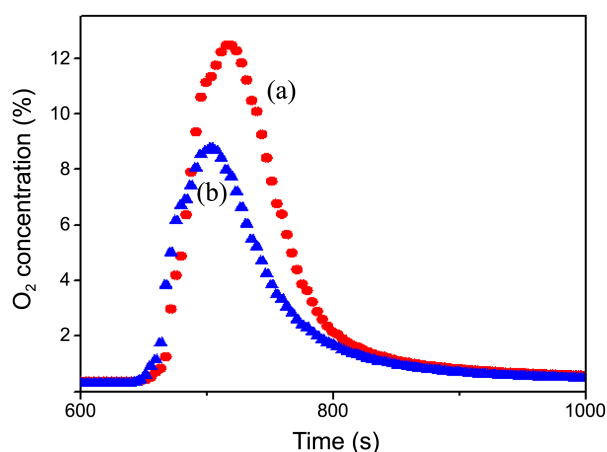


Figure 12. Oxygen desorption curves of powders synthesized through different methods: (a) SCF182 prepared *via* EDTA–citrate complex gel method; (b) SCF182 prepared *via* liquid citrate used in reference 17.

bution shown by ESEM images also reflect the change in surface area values (Table 4). The $\text{SrCo}_{0.8}\text{Fe}_{0.2}\text{O}_{3-\delta}$ powders prepared by the EDTA method have larger BET surface area ($40.396 \text{ m}^2/\text{g}$) than those prepared through the liquid citrate method. Surface area and porosity are important factors affecting gas–solid reactions. Particles with relatively smaller size and larger surface area can improve oxygen adsorption/desorption performance. Figure 12 depicts the oxygen desorption curves of $\text{SrCo}_{0.8}\text{Fe}_{0.2}\text{O}_{3-\delta}$ synthesized *via* different methods. The samples prepared through the EDTA method possess have more improved oxygen production properties than those prepared through the liquid citrate method. This behavior can be associated with the microstructure and morphology of $\text{SrCo}_{0.8}\text{Fe}_{0.2}\text{O}_{3-\delta}$ *via* the two synthesis methods. In conclusion, the synthesis method is an important factor for the improvement of oxygen production performance of perovskite-type oxygen carriers. The effects and optimization of the process parameters of the EDTA–citrate complex gel method on the performance of $\text{SrCo}_{0.8}\text{Fe}_{0.2}\text{O}_{3-\delta}$ need further investigation.

Conclusion

In this study, $\text{SrCo}_{1-x}\text{Fe}_x\text{O}_{3-\delta}$ powders with improved O_2/CO_2 production performance for oxyfuel combustion system were investigated through micro-characteristic and fixed-bed experiments measurements. The effects of Co doping and different synthesis methods are also investigated and reported. The following conclusions can be drawn from this study:

1. For a fixed A-site composition of $\text{SrCo}_{1-x}\text{Fe}_x\text{O}_{3-\delta}$, the different x values of $\text{SrCo}_{1-x}\text{Fe}_x\text{O}_{3-\delta}$ have no obvious effects on crystalline structure. However, the oxygen desorption performance of $\text{SrCo}_{1-x}\text{Fe}_x\text{O}_{3-\delta}$ is improved by Co doping.

2. $\text{SrCo}_{0.8}\text{Fe}_{0.2}\text{O}_{3-\delta}$ has significantly higher performance than $\text{La}_{0.1}\text{Sr}_{0.9}\text{Co}_{0.5}\text{Fe}_{0.5}\text{O}_{3-\delta}$ and $\text{Sr}_{0.5}\text{Ca}_{0.5}\text{Co}_{0.5}\text{Fe}_{0.5}\text{O}_{3-\delta}$ on cyclic

oxygen desorption. And multiple cycles demonstrated that $\text{SrCo}_{0.8}\text{Fe}_{0.2}\text{O}_{3-\delta}$ also displays high stability and regeneration capacity.

3. The synthesis method has significant effect on the performance of $\text{SrCo}_{0.8}\text{Fe}_{0.2}\text{O}_{3-\delta}$. The $\text{SrCo}_{0.8}\text{Fe}_{0.2}\text{O}_{3-\delta}$ powders prepared by the EDTA method have larger BET surface area ($40.396 \text{ m}^2/\text{g}$) than those prepared through the liquid citrate method.

Acknowledgments. The authors acknowledge the financial supports of National Basic Research Program of China (No. 2011CB707301), and the National Natural Science Foundation of China (No. 50936001, 51276078, 51021065). The authors are also grateful to Analytical and Testing Center of Huazhong University of Science and Technology for XRD and ESEM measurements.

References

- Herzog, H. *Environ. Sci. Technol.* **2001**, *35*, 148A.
- Luo, C.; Zheng Y.; Yin, J. J.; Qin, C. L.; Ding, N.; Zheng, C. G.; Feng, B. *Energy Fuels* **2013**, *27*, 1008.
- Liu, H.; Yuan, Y.; Yuan, X.; Yao, H. *Energy Fuels* **2012**, *26*, 829.
- Yang, Q.; Lin, Y. S.; Bulow, M. *AIChE J.* **2006**, *52*, 574.
- Croiset, E.; Thambimuthu, K. V. *Fuel* **2001**, *80*, 2117.
- Buhre, B. J. P.; Elliott, L. K. *et al. Prog. Energ. Combust.* **2005**, *31*, 283.
- Lee, S. H.; Kim, I. Y.; Kim, T. W.; Hwang, S. J. *Bull. Korean Chem. Soc.* **2008**, *29*, 817.
- Lee, W. J.; Yeo, H. J.; Kim, D. Y.; Paek, S. M. *Bull. Korean Chem. Soc.* **2013**, *34*, 2041.
- Jang, J. S.; Borse, P. H.; Lee, J. S.; Jung, O.; Cho, C. R.; Jeong, E. D.; Ha, M. G.; Won, M. S.; Kim, H. G. *Bull. Korean Chem. Soc.* **2009**, *30*, 1738.
- Borse, P. H.; Cho, C. R.; Yu, S. M.; Yoon, J. H.; Hong, T. E.; Bae, J. S.; Jeong, E. D.; Kim, H. G. *Bull. Korean Chem. Soc.* **2012**, *33*, 3407.
- Kim, W. H.; Son, J. Y. *Bull. Korean Chem. Soc.* **2013**, *34*, 2563.
- Yang, Z. H.; Lin, Y. S. *Ind. Eng. Chem. Res.* **2003**, *42*, 4376.
- Yang, Q.; Lin, Y. S. *AIChE J.* **2006**, *52*, 574.
- Yang, Q.; Lin, Y. S. *Ind. Eng. Chem. Res.* **2007**, *46*, 6025.
- Shao, Z. P.; Xiong, G. X. *Sep. Purif. Technol.* **2001**, *25*, 419.
- Tan, L.; Yang, Y. *AIChE J.* **2004**, *50*, 701.
- Rui, Z. B.; Ding, J. J.; Li, Y. D. *Fuel* **2010**, *89*, 1429.
- Shao, Z.; Haile, S. M. *Nature* **2004**, *431*, 170.
- Wang, H.; Tablet, C.; Feldhoff, A.; Caro, J. *J. Membrane Sci.* **2005**, *262*, 20.
- Rietveld, H. M. *J. Appl. Crystallogr.* **1969**, *2*, 65.
- Finger, L. W.; Cox, D. E.; Jephcoat, A. P. *J. Appl. Crystallogr.* **1994**, *27*, 892.
- Lee, S.; Lima, Y.; Lee, E. A. *J. Power Sources* **2006**, *157*, 848.
- Zhou, W.; Shao, Z.; Ran, R.; Chen, Z. *Electrochim. Acta* **2007**, *52*, 6297.
- Zhao, H.; Shen, W.; Zhu, Z.; Li, X.; Wang, Z. *J. Power Sources* **2008**, *182*, 503.
- Tan, L.; Gu, X.; Yang, L.; Zhang, L. *Sep. Purif. Technol.* **2003**, *32*, 307.
- Tan, L.; Gu, X.; Yang, L.; Jin, W.; Zhang, L.; Xu, N. *J. Membrane Sci.* **2003**, *212*, 157.
- Sun, X.; Li, S.; Sun, J.; Liu, X.; Zhu, B. *Int. J. Electrochem. Sci.* **2007**, *2*, 462.
- Saradha, S. T.; Muzhumathi, S. *J. Power Sources* **2007**, *165*, 728.